Anthropogenic and meteorological drivers of 1980–2016 trend in aerosol optical and radiative properties over the Yangtze River Basin

Lijie He [a], Lunche Wang [b,c,*], Bo Huang [a,**], Jing Wei [d,e], Zhigao Zhou [f], Yang Zhong [f]

[a] Department of Geography and Resource Management, The Chinese University of Hong Kong, Shatin, 999077, Hong Kong, China
[b] Hubei Key Laboratory of Critical Zone Evolution, School of Geography and Information Engineering, China University of Geosciences, Wuhan, 430074, China
[c] Key Laboratory of Middle Atmosphere and Global Environment Observation (LAGEO), Institute of Atmospheric Physics, Chinese Academy of Sciences, Beijing, 100029, China
[d] State Key Laboratory of Remote Sensing Science, College of Global Change and Earth System Science, Beijing Normal University, Beijing, China
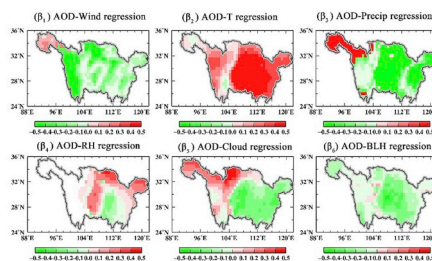[e] Department of Atmospheric and Oceanic Science, Earth System Science Interdisciplinary Center, University of Maryland, College Park, MD, USA
[f] School of Resource and Environmental Science, Wuhan University, Wuhan, Hubei Province, 430079, China

HIGHLIGHTS

- The over-increasing trends in AOD and ADRE were curbed around 2010.
- Changes in emissions dominated the growth of AOD and ADRE after 1980.
- The expansion of built-up land accelerated the growth of AOD and ADRE.
- A compact urban form was conductive to reducing AOD and ADRE.
- The temperature rise has led to a growth of AOD by 0.00084 per year since 1980.

GRAPHICAL ABSTRACT

Regression coefficients of AOD and meteorlogical condition based on MLR model.

ARTICLE INFO

ABSTRACT

Since the reform and opening up, Yangtze River Basin (YRB) with rapid industrialization and urbanization has become the most important source of anthropogenic aerosol emissions. However, the drivers of long-term trends in aerosol optical and radiative properties have not yet been adequately clarified. In this study, the multiple linear regression (MLR) and geographically weighted regression (GWR) models were employed to quantitatively estimate the impact of anthropogenic emissions, land use cover changes, urban forms and meteorological conditions on aerosol optical depth (AOD) and direct radiative effect (ADRE). A trend analysis revealed that over-increasing trends in AOD and ADRE were curbed around 2010. In addition, there were remarkable regional differences with respect to the effects of anthropogenic and meteorological factors on aerosol trends. Anthropogenic emissions dominated the growth of AOD and ADRE in the middle and lower reaches of the YRB after 1980, but not in the source of the YRB. Besides, the expansion of built-up land (at a 5.79% rate of increase) during 1980–2010 mainly occurred in the YRD, CC, and SB, which thus accelerated the growth of AOD and ADRE. Furthermore, AOD-ADRE was positively related to the patch area (CA), patch number (NP), and patch edge density (ED), but negatively associated with the largest patch index (LPI). It indicated that a compact urban

* Corresponding author. Hubei Key Laboratory of Critical Zone Evolution, School of Geography and Information Engineering, China University of Geosciences, Wuhan, 430074, China.
** Corresponding author.
E-mail addresses: wang@cug.edu.cn (L. Wang), bohuang@cuhk.edu.hk (B. Huang).

form could mitigate aerosol loadings by enhancing urban connectivity and reducing vehicle dependence. Finally, a rise in temperature was found to be one of the driving factors for AOD growth. However, the theoretical growth in AOD (0.00084 yr^{-1}) in relation to temperature rise was far less than the actual growth (0.0065 yr^{-1}).

1. Introduction

Although aerosols account for only one billionth of the total atmosphere, they play an important role in regional and global climate change, atmospheric environment, and human health (Remer and Kaufman, 2006; Wei et al., 2019a, b). IPCC (2013) clearly stated that aerosols were the most unstable climate change factor in the atmosphere-earth interaction. Since the reform and opening up (1980 onwards), Yangtze River Basin (YRB) has witnessed a rapid urban expansion process and thus has become the largest source of anthropogenic aerosol emissions (Xia et al., 2016; He et al., 2018a, 2018b, 2019a). However, the long-term trends in aerosols and their underlying causes have not been well understood.

In recent years, extensive efforts have been made to estimate spatiotemporal trends in aerosol optical depth (AOD) and its direct radiative effect (ADRE) in China (Kuang et al., 2015; He et al., 2016; Alfaro et al., 2017; Zhang et al., 2017; Che et al., 2019; Wei et al., 2019c). However, due to the lack of ground-based and remote sensing data, the AOD trend before 2000 could not be observed and there was no conclusion in long-term AOD and ADRE trends. For example, He et al. (2016) found a significant upward (downward) MODIS AOD trend in China during 2000–2008 (2009–2016), together with an average rate of 0.0003 (-0.0005) per month. But Li and Wang (2014) revealed a continuous downward AOD trend in both Xianghe (2002–2015) and Beijing (2005–2012) using AERONET datasets. In addition, De Leeuw et al. (2017) found a downward trend in MODIS AOD from 2006 to 2009 in China, but ATSR (Along Track Scanning Radiometers) AOD did not show a downward trend in the same period. To provide greater information about long-term trends, the aim of the current study was to estimate the long-term AOD and ADRE trends (1980 onwards) in the YRB using monthly MERRA-2 aerosol datasets.

In terms of the underlying causes of aerosol trend, most previous researches confirmed that anthropogenic emissions were the main reason for the continuous increase of aerosols in China (Deng et al., 2008; Gao et al., 2011; Guo et al., 2016; Liu et al., 2019). For example, Deng et al. (2008) showed that AOD in the Pearl River Delta was significantly enhanced during biomass burning in Southeast Asia. Gao et al. (2011) found that due to the implementation of a series of emission control measures, the aerosol concentrations during the Beijing Olympic Games decreased by 30%–50% compared with the same period of 2007. Furthermore, Guo et al. (2016) also observed that based on the WRF-Chem model, the local emission reductions in Beijing during the 2014 APEC meeting contributed more to Beijing's air quality improvement than those outside Beijing. However, they neglected the impact of land use cover change (LUCC) and urban form change on the long-term aerosol trend. In the past 40 years, China has witnessed profound land use cover changes (Liu et al., 2005, 2019; Ge et al., 2019). More and more scholars advocated that urban expansion characterized by changes in land use and urban forms had a significant impact on aerosol trends (Clark et al., 2011; McCarty and Kaza, 2015; Fan et al., 2018). She et al. (2017) found that MODIS AODs were closely related to LUCC in major cities in China. Wang et al. (2016) reported that LUCC and anthropogenic emissions were the dominant reasons for the spatiotemporal distribution of AOD in the Ebinur Lake Basin. Recently, Fan et al. (2018) also found that based on MLR and GWR models, a more compact and less fragmented urban form could effectively reduce urban air pollution in 344 prefecture-level cities of China.

However, previous studies have often focused on the effect of local meteorological conditions on aerosol pollution over short time periods, such as daily or seasonal changes. But it ignored the effect on long-term trends in AOD and ADRE (Westervelt et al., 2016; Wang et al., 2018). For instance, Tai et al. (2010) revealed that changes in meteorological conditions (including wind speed, temperature, relative humidity, and precipitation) could account for up to 50% of PM$_{2.5}$ daily changes in United States. Kuang et al. (2016) also reported that due to the hygroscopicity of aerosols, the instantaneous ADRE at the top of atmosphere increased by about 60% at high relative humidity over the North China Plain in summer.
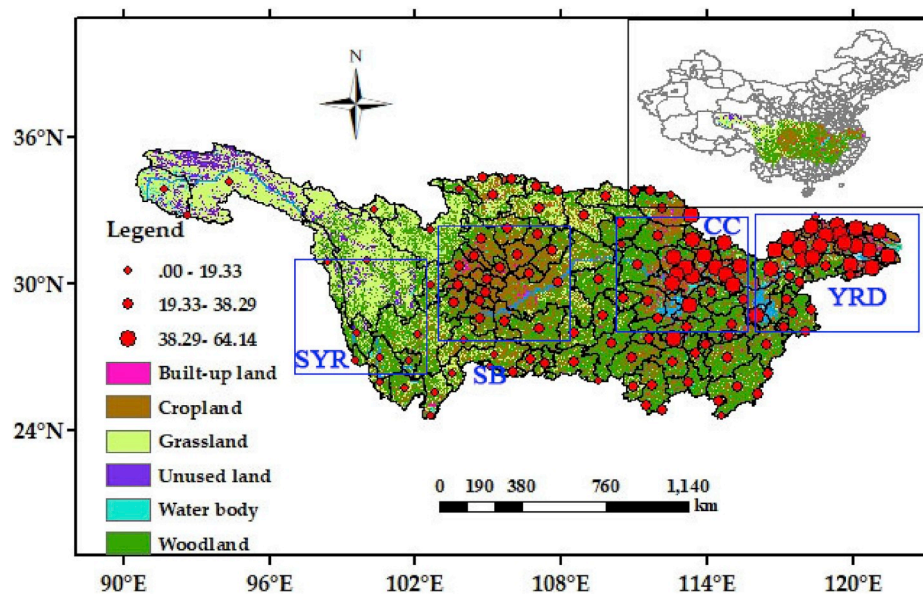

Fig. 1. Land use pattern and PM$_{2.5}$ pollution (red symbols) in the Yangtze River Basin. PM$_{2.5}$ data were derived from 476 state-controlled air quality monitoring stations (http://113.108.142.147:20035/emcpublish/). (For interpretation of the references to colour in this figure legend, the reader is referred to the Web version of this article.)
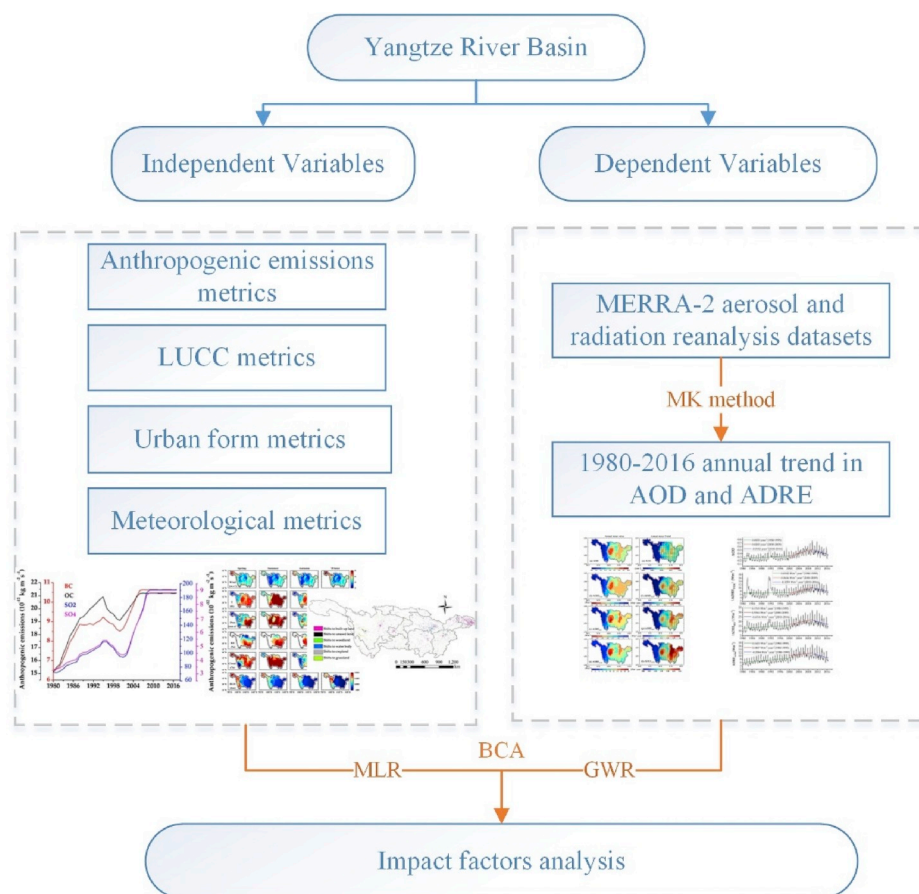
Fig. 2. Flow chart of study process.

Despite the importance of previous studies, the underlying factors behind long-term AOD and ADRE trends have not yet been fully explored. Given such limitations of existing research, this study was conducted to (1) accurately estimate the long-term trends in AOD and ADRE over the YRB during 1980–2016 using MERRA-2 aerosol datasets; (2) further explore the quantitative impact of anthropogenic emissions, land use cover changes and urban forms on 1980–2016 AOD-ADRE trend; and (3) finally determine whether local meteorological conditions (including surface wind speed (WS), temperature, precipitation, relative humidity (RH), total cloud cover, and the boundary layer height (BLH)) affect the AOD trend. The structure was organized as follows. Section 2 introduced study area, data and analytical methods. Section 3 analyzed the long-term trends of AOD and ADRE and their underlying factors. Finally, conclusions and policy implication were provided in Section 4.

2. Study area, data, and methodology

2.1. Study area

The Yangtze River Basin (YRB) is defined as the catchment area of the Yangtze River water system and the area through which it flows (90°E–122°E, 24°N-35°N). The YRB was selected as the region of interest for several reasons. First, as one of the fastest growing regions supporting China's economy, the YRB experienced severe air pollution, and approximately 87.10% of the cities in the YRB experienced annual mean $PM_{2.5}$ concentrations exceeding the WHO standard (20 μg/m^3) in 2016 (Fig. 1), particularly over the Yangtze River Delta (YRD), Central China (CC), and the Sichuan Basin (SB). Second, there were various aerosol sources within the different sub-regions of the YRB. For example, fine-mode aerosols were dominant in densely populated sub-regions

(YRD, CC, and SB), whereas coarse-mode aerosols primarily occurred in the source of the Yangtze River Basin (SYR) (Wang et al., 2015; He et al., 2017). Finally, the YRB has experienced rapid urbanization over the past 40 years, resulting in dramatic changes in land use coverage (Ge et al., 2019). In this context, it is critical to analyze the anthropogenic and meteorological drivers of aerosol pollution over the YRB.

2.2. Data and processing methods

As shown in Fig. 2, the YRB was divided into grid cells measuring 0.5° × 0.625° (latitude × longitude). First, the annual trends in AOD and ADRE within each grid rectangle from 1980 to 2016 were estimated using the MK method. The independent variables, namely anthropogenic emissions metrics, land use cover change (LUCC) metrics, urban form metrics, and meteorological metrics were calculated in ArcGIS 10.1 and FRAGSTATS 4.2. Finally, based on the bivariate correlation analysis (BCA), multiple linear regression (MLR), and geographically weighted regression (GWR), the effects of anthropogenic and meteorological metrics on AOD and ADRE trends were further explored.

2.2.1. Estimations of AOD and ADRE trends

AOD data used in this study was derived from the MERRA-2 aerosol reanalysis dataset (MERRA2_100.tavgM_2d_aer_Nx, Table S1). The MERRA-2 product was newly released by the NASA Global Modeling and Assimilation Office (GMAO) in 2017. Because of assimilating a series of bias-corrected AOD retrieves from MODIS, MISR, AVHRR and AERONET instruments, the MERRA-2 AOD agreed well with ground-based observations (Buchard et al., 2017). For example, the correlation coefficients between MERRA-2 AOD and AERONET AOD were 0.88, 0.84 and 0.90, respectively in Beijing, XiangHe and YRB (Randles et al., 2017; He et al., 2018b, 2019a). Such high agreements gave us enough

Table 1
LUCC transformation matrix used in this study.

		T_2				P_{i+}	Percentage Reduction (%)
		A_1	A_2	...	A_n		
T_1	A_1	P_{11}	P_{12}	...	P_{1n}	P_{1+}	P_{1+}-P_{11}
	A_2	P_{21}	P_{22}	...	P_{2n}	P_{2+}	P_{2+}-P_{22}
	⋮	⋮	⋮	⋮	⋮	⋮	⋮
	A_n	P_{n1}	P_{n2}	...	P_{nn}	P_{n+}	P_{n+}-P_{nn}
P_{+j}		P_{+1}	P_{+2}	...	P_{+n}	1	
Percentage increase (%)		P_{+1}-P_{11}	P_{+2}-P_{22}	...	P_{+n}-P_{nn}		

Table 2
Calculation of urban form metrics in Fragstats4.2 software.

Index	Equation		Description
Patch Number (NP)	$NP = N_i$	(5)	i refers to built-up land type. N = number of built-up land patches. NP > 0 Unit:/.
Patch Area (CA)	$CA = \sum_{j=1}^{N_i} a_{ij}$	(6)	a_{ij} = area (ha) of each built-up land patch, j. CA > 0 Unit: ha.
Largest Patch Index (LPI)	$LPI = \dfrac{\max a_{ij}}{AREA} \times 100$	(7)	AREA = total landscape area (ha). 0 < LPI ≤ 100 Unit: %.
Edge Density (ED)	$ED = \dfrac{1}{AREA} \sum_{j=1}^{N_i} P_{ij}$	(8)	P_{ij} = Boundary length between patches of *type i* landscape (namely built-up land) and its adjacent patches of *type j* landscape. Unit: m/ha.

confidence in using MERRA-2 AOD reanalysis data for aerosol applications over the YRB.

ADRE data was derived from the MERRA-2 radiation reanalysis dataset (MERRA2_100.tavgM_2d_rad_Nx, Table S1). In clear sky, ADRE was defined as the difference in the net (downward ↓ minus upward ↑) shortwave radiation flux with and without aerosols at the top of atmosphere (TOA, Equation (1)), at the surface (SFC, Equation (2)) and within the atmosphere (ATM, Equation (3)).

$$ADRE_{TOA} = (F_{aero}\downarrow - F_{aero}\uparrow)_{TOA} - (F_{clr}\downarrow - F_{clr}\uparrow)_{TOA} \tag{1}$$

$$ADRE_{SFC} = (F_{aero}\downarrow - F_{aero}\uparrow)_{SFC} - (F_{clr}\downarrow - F_{clr}\uparrow)_{SFC} \tag{2}$$

$$ADRE_{ATM} = ADRE_{TOA} - ADRE_{SFC} \tag{3}$$

where $(F_{aero}\downarrow - F_{aero}\uparrow)$ and $(F_{clr}\downarrow - F_{clr}\uparrow)$ are the net shortwave radiation flux with and without aerosols, respectively (He et al., 2018b). If ADRE >0, aerosols exert a warming effect on the TOA, SFC, and ATM; otherwise there is a cooling effect.

2.2.2. Pretreatment of anthropogenic emission metrics

The anthropogenic emissions were generally considered to be the dominant factors for the long-term change of aerosol optical-radiation characteristics in China (Guo et al., 2016). Therefore, four anthropogenic emissions from the MERRA-2 reanalysis dataset (MERRA2_100.tavgM_2d_adg_Nx, Table S1) were selected as independent variables, including SO_2, SO_4, black carbon (BC) and organic carbon (OC). Based on the bivariate correlation analysis (Equation (4)), the Pearson correlation coefficients (r) between anthropogenic emissions (x_i) and AOD-ADRE (y_i) were calculated in each $0.5° \times 0.625°$ grid.

$$r = \frac{\sum_{i=1}^{n}(x_i - \bar{x})(y_i - \bar{y})}{\sqrt{\sum_{i=1}^{n}(x_i - \bar{x})^2 \sum_{i=1}^{n}(y_i - \bar{y})^2}} \tag{4}$$

2.2.3. Pretreatment of LUCC metrics

The 1 km × 1 km land use cover data were provided by the Resource and Environmental Science Data Center, CAS (Table S1). The dataset was generated by artificial visual interpretation from seven Landsat TM/ETM remote sensing images of 1980, 1990, 1995, 2000, 2005, 2010, and 2015. Land cover types were divided into six primary types and 25 secondary types, including cropland, woodland, grassland, water body, built-up land, and unused land. The specific classification system could be found at http://www.resdc.cn/data.aspx?DATAID=95.

Since economic reform and the introduction of the Open-Door policy, China's rapid urban expansion process has caused profound land use changes, which has played an important role in urban air pollution. (Liu et al., 2005; Li and Wang, 2014). In this study, the LUCC types between 1980 and 2015 were further estimated using a LUCC transformation matrix in ArcGIS 10.1 (Table 1). As shown in Table 1, lines A_1 … A_n represent the types of land cover in T_1 year, and columns A_1 … A_n represent the types of land cover in T_2 year. Furthermore, P_{11} … P_{nn}

represents the percentage area where land cover type, n, remains unchanged from T_1 to T_2; P_{i+} represents the total area percentage of land cover type i in T_1 year; P_{+j} represents the total area percentage of land cover type j in T_2 year; P_{i+}-P_{ii} represents the percentage area decrease in land cover type, i, from T_1 to T_2; and P_{+j}-P_{ii} represents the percentage area increase in land cover type, j, from T_1 to T_2.

2.2.4. Pretreatment of urban form metrics

Urban form represented the spatial allocation of urban landscape (Larkin et al., 2016). Previous studies often used population density (PD) as a measure of urban form. However, urban population density alone was not enough, and a more comprehensive urban form indicator system needed to be constructed (McCarty and Kaza, 2015; Fan et al., 2018). In this study, four urban form metrics, namely, the patch area (CA), patch number (NP), largest patch index (LPI) and patch edge density (ED), were selected to characterize the fragmentation and compactness of a city. As shown in Table 2, CA is an important indicator used to measure urban expansion, and there is no upper limit to its value. It is generally believed CA increases with the expansion of a city (Wang et al., 2017). NP indicates the number of built-up land patches and also has no upper limit. She et al. (2017) revealed that the increase of NP would lead to the increase of urban fragmentation. LPI is a very important parameter used to measure urban compactness, and its value ranges from 0 to 100. Previous studies found that the increase of LPI would lead to the improvement of urban compactness (McCarty and Kaza, 2015; Fan et al., 2018). Finally, ED measures the total length of all edge segments related to a given urban patch. Wang et al. (2017) reported that the larger the ED, the stronger the urban heterogeneity.

In this study, by using built-up land data from the 7 Landsat TM remote sensing images (1980, 1990, 1995, 2000, 2005, 2010 and 2015), the four urban form metrics in 121 cities of the YRB were calculated in Fragstats4.2 software based on Equation (5)- (8). The calculation results were shown in Fig. S2. In addition, MLR (Equation (9)) and GWR (Equations (10) and (11)) models were selected to estimate the quantified effect of urban form metrics on aerosol optical and radiative properties.

$$y = \beta_0 + \sum_{i=1}^{p} \beta_i x_i + \varepsilon_i \tag{9}$$

where the dependent variable, y, represents the annual mean AOD and ADRE in each city; independent variables x_i, represent the four urban form metrics; β_0 is a constant term, and ε_i is an interaction term. The slope coefficient, β_i, can be interpreted as the sensitivity of AOD to changes in one urban form metric, which assumes that the other urban
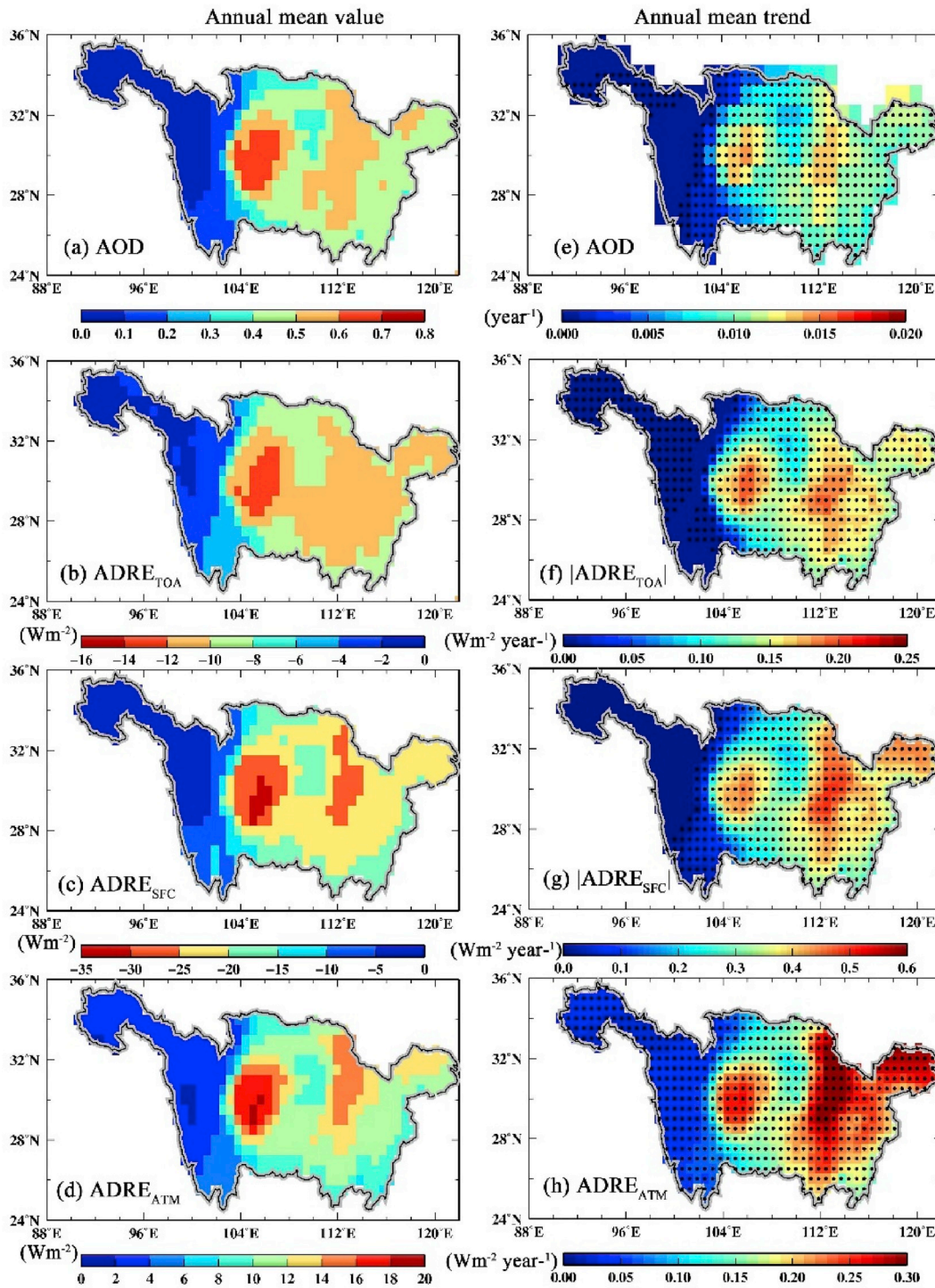
Fig. 3. Spatial distribution (left) and spatial trend analysis (right) of AOD and ADRE in the YRB from 1980 to 2016.

form metrics held fixed, and it can be determined via a least-square adjustment. Furthermore, per capita GDP (PGDP), PD, precipitation (Prec), and temperature (T) were selected as the control variables. MLR model calculations were conducted using SPSS19.0 software.

Compared with MLR model, the GWR model could detect local spatial variations among variables by setting weight matrix (Fan et al., 2018). The GWR equations were as follows.

$$y_j = \beta_0(u_j, v_j) + \sum_{i=1}^{p} \beta_i(u_j, v_j)x_{ij} + \varepsilon_j \quad (10)$$

where y_j represents the annual mean AOD and ADRE values, u_j and v_j are the longitude and latitude coordinates of prefecture-level city j, respectively, $\beta_0(u_j, v_j)$ is the intercept, x_{ij} is the UF of independent variables, $\beta_i(u_j, v_j)$ is the regression coefficient, and ε_j is the error term. The weight matrix used in the GWR model could be expressed by Equation (11):

$$\beta_f(u_j, v_j) = (X^T W(u_j, v_j)X)^{-1} X^T W(u_j, v_j)y \quad (11)$$

All calculations of GWR models could be completed in ArcGIS 10.1 software. Noncollinearity and AIC minimization were selected as
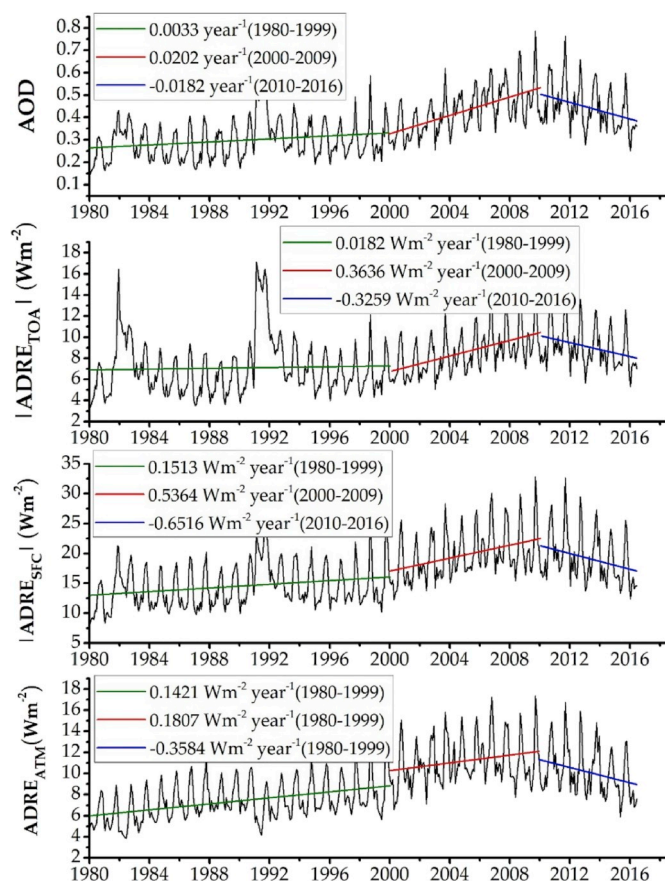
Fig. 4. Staged trend analysis of AOD and ADRE over the YRB from 1980 to 2016.

criteria. The significance of the model was tested by variance analysis (F test) and the significance of local parameters was evaluated by the *t*-test (Fan et al., 2018).

2.2.5. Pretreatment of meteorological metrics

Local meteorological conditions had profound effect on seasonal and daily variations of AOD and ADRE (Wang et al., 2018; Zhou et al., 2017, 2018). In this study, six meteorological factors were selected as independent variables, including surface wind speed (m s^{-1}), total cloud amount (%), surface temperature (K), relative humidity (%), precipitation (mm day^{-1}), and boundary layer height (m) (Table S1). The multiple linear regression (MLR) model was used to quantify the relationship between meteorological conditions and aerosol pollution.

3. Results and discussion

3.1. Long-term trends in AOD and ADRE

Fig. 3 showed the annual mean values (left) of AOD and ADRE over the YRB during 1980–2016. Obviously, AOD had significant spatial heterogeneity, which high values (AOD > 0.5) occurred in YRD, CC and SB. In these regions, frequent urbanization and industrialization activities took place, resulting in considerable anthropogenic aerosol emissions. Since ADRE$_{TOA}$ and ADRE$_{SFC}$ were all negative, the aerosols exerted cooling effects at the top of atmosphere and the surface. However, there was a warming effect of aerosol within the atmosphere. The spatial distributions of ADRE were consistent with those of AOD.

Fig. 3 also showed the annual mean trends (right) of AOD and ADRE over the YRB during 1980–2016. Black dots indicated trends of AOD and ADRE above the 95% significance level (P < 0.05), which were detected
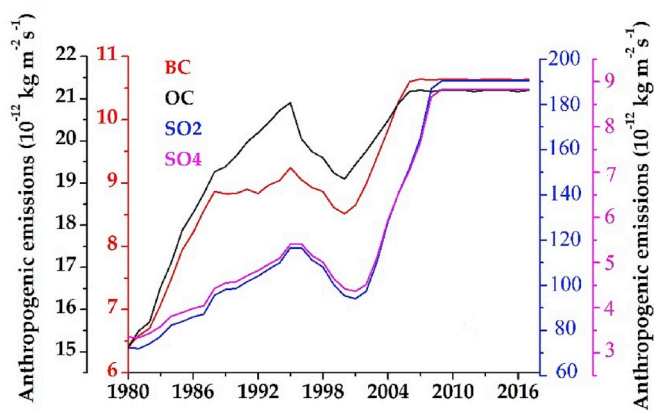

Fig. 5. Anthropogenic emission trends over YRB from 1980 to 2016.

by the MK method. Furthermore, AOD, |ADRE$_{TOA}$|, |ADRE$_{SFC}$|, and ADRE$_{ATM}$ all had a significant upward trend, particularly in the YRD, CC, and SB.

Fig. 4 illustrated the staged trends in regionally averaged AOD and ADRE since 1980. Prior to 2000, trends in AOD, |ADRE$_{TOA}$|, |ADRE$_{SFC}$|, and ADRE$_{ATM}$ depicted slight increases, with annual mean increased trends of 0.003 year^{-1}, 0.02 Wm^{-2} year^{-1}, 0.15 Wm^{-2} year^{-1}, and 0.14 Wm^{-2} year^{-1}, respectively. Notably, both AOD and ADRE suffered from an abnormal growth in 1982 and 1991, probably due to the eruptions of El Chichon in Mexico and the Pinatubo in the Philippines, respectively (Dutton and Christy, 1992). During 2000–2009, there were significant growth trends for AOD, |ADRE$_{TOA}$|, |ADRE$_{SFC}$|, and ADRE$_{ATM}$, with annual mean growth trends of 0.02 year^{-1}, 0.36 Wm^{-2} year^{-1}, 0.54 Wm^{-2} year^{-1}, and 0.18 Wm^{-2} year^{-1}, respectively. However, these over-increased trends of AOD and ADRE were curbed around 2010. During 2010–2016, AOD, |ADRE$_{TOA}$|, |ADRE$_{SFC}$| and ADRE$_{ATM}$ underwent annual mean downward trends of −0.02 year^{-1}, -0.33 Wm^{-2} year^{-1}, -0.65 Wm^{-2} year^{-1}, and -0.36 Wm^{-2} year^{-1}, respectively. Recently, studies using multi-source remote sensing and ground-based datasets have also observed a downward trend in AOD in China after 2008. For example, He et al. (2016) observed a downward trend in AOD (−0.005 month^{-1}) after 2008 using the MODIS 3 km product. Zhang et al. (2017) found a significant decreasing trend in AOD in southeast and northeast coastal areas of China during 2009–2015, together with annual average decline rates of 8% and 7%, respectively. The decrease in AOD after 2010 could be related to the staging of the 2008 Olympics in Beijing and the 2008 global economic crisis, which resulted in the implementation of a series of energy saving and emission reduction measures in China (He et al., 2016).

3.2. Effect of anthropogenic emissions on AOD and ADRE trends

Fig. 5 showed 1980–2016 trends in black carbon (BC), organic carbon (OC), SO$_2$ and SO$_4$ anthropogenic emissions over the YRB. Obviously, the over-increasing trends of four anthropogenic emissions were curbed around 2008–2010, which were consistent with those of AOD and ADRE. To clarify the relationship between aerosol pollution and anthropogenic emissions, Pearson correlation coefficients (r) between BC, OC, SO$_2$, SO$_4$ emissions and AOD were calculated for each 0.5° × 0.625° grid (Fig. 6). The black dots represent r values passing the 95% significant level detected by the *t*-test method (P < 0.05). As shown in Fig. 6, the r values showed significant spatial differentiation. High correlations between BC, OC, SO$_2$, SO$_4$ emissions and AOD (r > 0.6) occurred in the middle and lower reaches of the YRB, together with regional averaged r values of 0.78、0.70、0.73 and 0.75, respectively. On the contrary, low correlations (r < 0.4) appeared in the SYR, together with regional averaged r values of 0.31、0.26、0.33 and 0.25. Furthermore, Fig. S1 – S3 showed correlations of |ADRE$_{TOA}$|, |ADRE$_{SFC}$|,
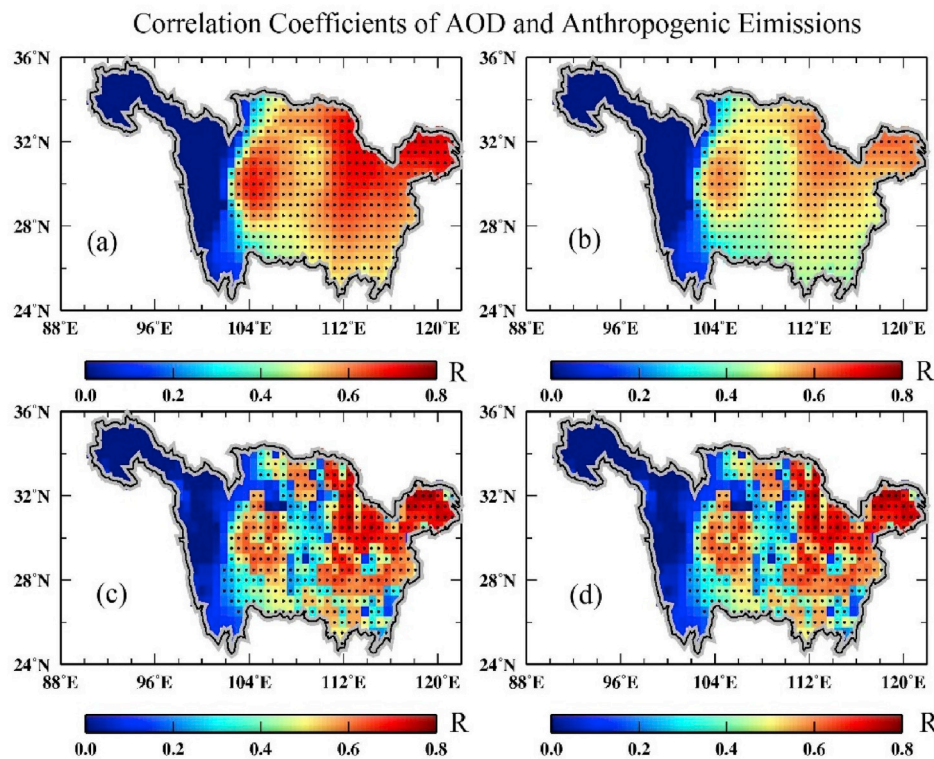
Fig. 6. Correlation coefficients between AOD and anthropogenic emissions (a) BC, (b) OC (c) SO_2 and (d) SO_4 determined using bivariate correlation method.
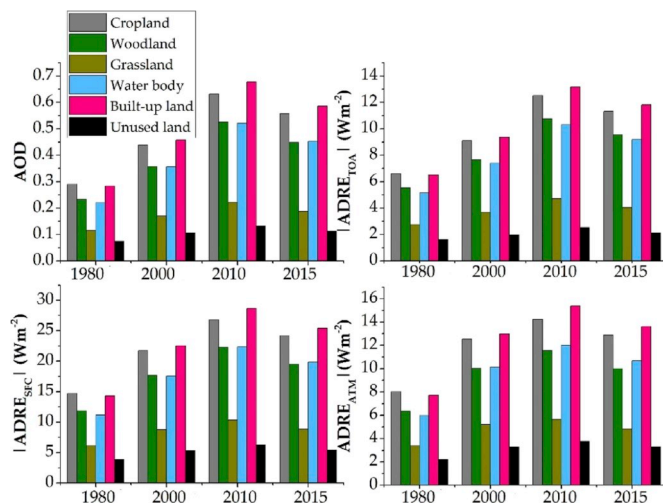

Fig. 7. Annual mean AOD and ADRE values for six primary land use cover types.

$ADRE_{ATM}$ and anthropogenic emissions. Their spatial distributions were similar to AOD. This indicated that anthropogenic emissions could be the dominant factors for the changes in AOD and ADRE over the middle and lower reaches of the YRB, but not over the SYR. Due to the low population density and the infrequent industrialization and urbanization, natural aerosols dominated in the SYR, weakening the effect of anthropogenic emissions on aerosol loadings.

3.3. Effect of LUCC on AOD and ADRE trends

Fig. 7 showed annual mean AOD and ADRE values of six primary land use cover types in 1980, 2000, 2010 and 2015. It was not difficult to see that the annual mean AOD and ADRE values for all land use types

increased during 1980–2010, but decreased during 2010–2015. Specially, the AOD, $|ADRE_{TOA}|$, $|ADRE_{SFC}|$ and $ADRE_{ATM}$ values in built-up land were highest, with a multi-year average of 0.48 ± 0.15, 10.21 ± 2.53 Wm^{-2}, 22.71 ± 5.31 Wm^{-2} and 12.43 ± 2.85 Wm^{-2}, respectively (Table 3). On the contrary, the AOD and ADRE values in unused land and grass land were relatively low. The reason might be that the unused land and grass land were mostly located in the SYR (Fig. 1). The region had a sparse population, slow urbanization and industrialization, resulting in low aerosol loadings. Notably, compared with the grass land, the AOD and ADRE values of the woodland were relatively high. This might be due to the fact that the Dark Target (DT) method used in MERRA-2 reanalysis easily overestimated AOD values in areas with low surface reflectance, such as woodlands (Randles et al., 2017; Buchard et al., 2017, He et al., 2018b). The AOD, $|ADRE_{TOA}|$, $|ADRE_{SFC}|$ and $ADRE_{ATM}$ values in permanent ice and snow land were lowest, with a multi-year average of 0.07 ± 0.01, 1.42 ± 0.19 Wm^{-2}, 3.80 ± 0.63 Wm^{-2} and 2.43 ± 0.47 Wm^{-2}, respectively (Table 3). However, the AOD and ADRE values of the other water body were relatively high, probably associated with the hygroscopicity growth of aerosols (Wang et al., 2015; Xia et al., 2016).

More and more researchers confirmed that land use cover changes had a profound effect on the global and regional air pollution (Clark et al., 2011; McCarty and Kaza, 2015). Therefore, this study attempted to portray the six primary land use cover changes over the YRB from 1980 to 2016 using the land use transformation matrix (Fig. S4). Note that 1 to 6 denoted the Cropland, Woodland, Grassland, Water body, Built-up land and Unused land, respectively. The land use trajectories with the same category in different time periods, such as 11, 22, 111, 222, 333, etc., represented patches without land use conversion. Other land use trajectories, such as 12, 23, 112, etc., represented patches with land use conversion (Liu et al., 2005). For example, 12 in Fig. S4 (top) referred to the land use conversion from cropland in 1980 to Woodland in 2010. 115 in Fig. S4 (bottom) referred to the land use conversion from cropland in 1980 to built-up land in 2015, but remained as cropland in 2010.

Table 3
Multi-year mean AOD and ADRE values for 25 secondary land use cover types from 1980 to 2015.

Land use cover type		AOD (/)		$|ADRE_{TOA}|$ (W m^{-2})		$|ADRE_{SFC}|$ (W m^{-2})		$|ADRE_{ATM}|$ (W m^{-2})	
		AVE	STD	AVE	STD	AVE	STD	AVE	STD
Cropland	Paddy land	0.47	0.14	10.16	2.37	22.16	4.68	11.98	2.39
	Dry land	0.46	0.12	9.61	2.14	21.53	4.36	11.88	2.31
Built-up land	Rural settlements	0.48	0.15	10.18	2.48	22.86	5.37	12.70	2.88
	Urban built-up	0.48	0.15	10.32	2.53	22.97	5.28	12.47	2.90
	others	0.47	0.15	10.14	2.58	22.31	5.30	12.12	2.79
Water body	Reservoir and ponds	0.49	0.15	10.46	2.60	23.31	5.50	12.79	2.97
	Stream and rivers	0.48	0.14	10.17	2.46	22.39	5.13	12.16	2.73
	Lakes	0.45	0.14	9.74	2.46	21.44	5.21	11.64	2.80
	Beach and shore	0.44	0.14	10.10	2.50	21.45	5.29	11.47	2.80
	Bottomland	0.29	0.09	6.15	1.49	13.94	3.18	7.75	1.72
	Permanent ice and snow	0.07	0.01	1.42	0.19	3.80	0.63	2.43	0.47
Woodland	Forest	0.41	0.12	8.91	2.08	18.99	4.06	10.09	2.05
	Shrub	0.37	0.11	8.28	1.95	17.40	3.79	9.16	1.89
	Woods	0.32	0.09	7.13	1.58	15.40	3.11	8.32	1.59
	Others	0.42	0.13	9.15	2.27	19.50	4.36	10.34	2.17
Grassland	Dense grass	0.24	0.06	5.43	1.10	11.74	2.25	6.36	1.18
	Moderate grass	0.19	0.04	4.28	0.80	9.51	1.69	5.26	0.93
	Sparse grass	0.08	0.01	1.67	0.24	4.33	0.67	2.68	0.44
Unused land	Swampland	0.19	0.05	3.99	0.77	9.31	1.76	5.30	1.00
	Bare soil	0.14	0.05	3.17	0.93	7.30	2.00	4.13	1.08
	Salina	0.08	0.01	1.46	0.15	4.17	0.65	2.67	0.44
	Bare rock	0.08	0.01	1.66	0.22	4.15	0.56	2.53	0.44
	Sandy land	0.08	0.01	1.35	0.14	3.84	0.48	2.49	0.37
	Gobi	0.08	0.01	1.37	0.16	3.87	0.54	2.49	0.41
	Others	0.08	0.01	1.45	0.19	3.86	0.56	2.41	0.38

AVE and STD refer to the averaged values of AOD-ADRE and their standard deviation values, respectively.

To better assess LUCCs in the YRB from 1980 to 2015, we further reclassified the major land use trajectories based on Fig. S4. The reclassification results were shown in Fig. 8. As observed, YRB had two main land use changes between 1980 and 2015, namely, the expansions of built-up land and grassland. The expansion of built-up land mainly occurred in the YRD, CC and SB, where the aerosol loadings also increased significantly. It could be inferred that the growth of AOD and ADRE in these regions from 1980 to 2015 were closely related to the expansion of built-up land. In addition, the expansion of grassland mainly appeared at the SYR, where there were no significant changes of AOD and ADRE.

As analyzed in section 3.1, there was a turn point around 2010, when the over-increasing trends of AOD and ADRE was curbed. Therefore, land use cover changes of the YRB were also analyzed during 1980–2010 (Table 4) and 2010–2015 (Table 5). The major land use change was the expansion of built-up land, with the change rates of 5.79% (1980–2010) and 1.96% (2010–2015), respectively. The expansion of built-up land mainly came from the conversion of cropland, theoretically leading to a growth of aerosol loading during the two periods. Notably, far less land conversion from cropland to built-up land (1.17%) occurred during 2010–2015 compared to the previous period (5.12%). The reason was associated with China's strict implementation of basic farmland protection policies in recent years (He et al., 2019b). In this context, the over-increasing trends in AOD and ADRE during 2010–2015 were effectively curbed. However, as analyzed in section 3.2, changes in anthropogenic emissions were the dominant factor for the downward trends of AOD and ADRE during 2010–2015.

3.4. Effect of urban form on AOD and ADRE trends

Table 6 showed the multiple linear regression (MLR) coefficients between AOD-ADRE and urban form metrics in 121 cities of the YRB from 1980 to 2015. In the MLR model, several socioeconomic and meteorological factors including per capita GDP (PGDP), population density (PD), precipitation (Prec) and temperature (T) were selected as control variables. All the adjusted determination coefficients (R^2) were

as high as 0.7, suggesting that the MLR models had good performance.

Regression coefficients revealed that AOD-ADRE were significantly correlated with the patch area (CA). A 1% increase in CA would lead to a growth in AOD, $|ADRE_{TOA}|$, $|ADRE_{SFC}|$ and $ADRE_{ATM}$ by 2.019E-7%、2.882E-6%、4.340E-6% and 1.462E-6%, respectively. Similarly, there was also a significantly positive relationship between AOD-ADRE and patch number (NP). A 1% increase in NP would result in an increase in AOD, $|ADRE_{TOA}|$, $|ADRE_{SFC}|$ and $ADRE_{ATM}$ by 6.778E-5%、0.001%、0.002% and 0.002%, respectively. The reason was likely that the high NP values would increase the fragmentation of a given city. As a result, there would be more vehicle kilometers of travel, which would further increase transportation-related nitrate aerosol emissions (Fan et al., 2018). On the contrary, the largest patch index (LPI) was negatively related to AOD and ADRE. A 1% increase in LPI would reduce AOD, $|ADRE_{TOA}|$, $|ADRE_{SFC}|$ and $ADRE_{ATM}$ by −0.09%、-0.125%、-0.385% and −0.26%, respectively. LPI represented the compactness of a given city. It was found that a compact urban form would help to alleviate local aerosol pollution by enhancing urban connectivity, reducing vehicle dependence and facilitating the use of bicycle and walk (McCarty and Kaza, 2015; Rodríguez et al., 2016; Fan et al., 2018). Recently, McCarty and Kaza (2015) reported that in the United States, compact cities usually had better air quality. Rodríguez et al. (2016) also found that PM$_{2.5}$ and NO$_2$ were positively related to the fragmentation of 249 large cities in Europe. However, the patch edge density (ED) was positively related to AOD and ADRE (p < 0.05). A 1% growth of ED would increase AOD, $|ADRE_{TOA}|$, $|ADRE_{SFC}|$ and $ADRE_{ATM}$ by 0.23%、0.363%、0.99% and 0.627%, respectively. A higher ED would increase irregularity of a city shape, thereby weakening urban connectivity, stimulating demand for vehicles and energy, and further increasing anthropogenic aerosol emissions. Wang et al. (2017) revealed that the continuous increase of carbon emissions in Beijing, Tianjin, Shanghai and Guangzhou cities was closely associated with the irregular pattern of urban land.

In order to address the spatial differentiation effect, a geographically weighted regression (GWR) model was further selected. Fig. 9 illustrated the adjusted determination coefficients (R^2) between AOD and urban
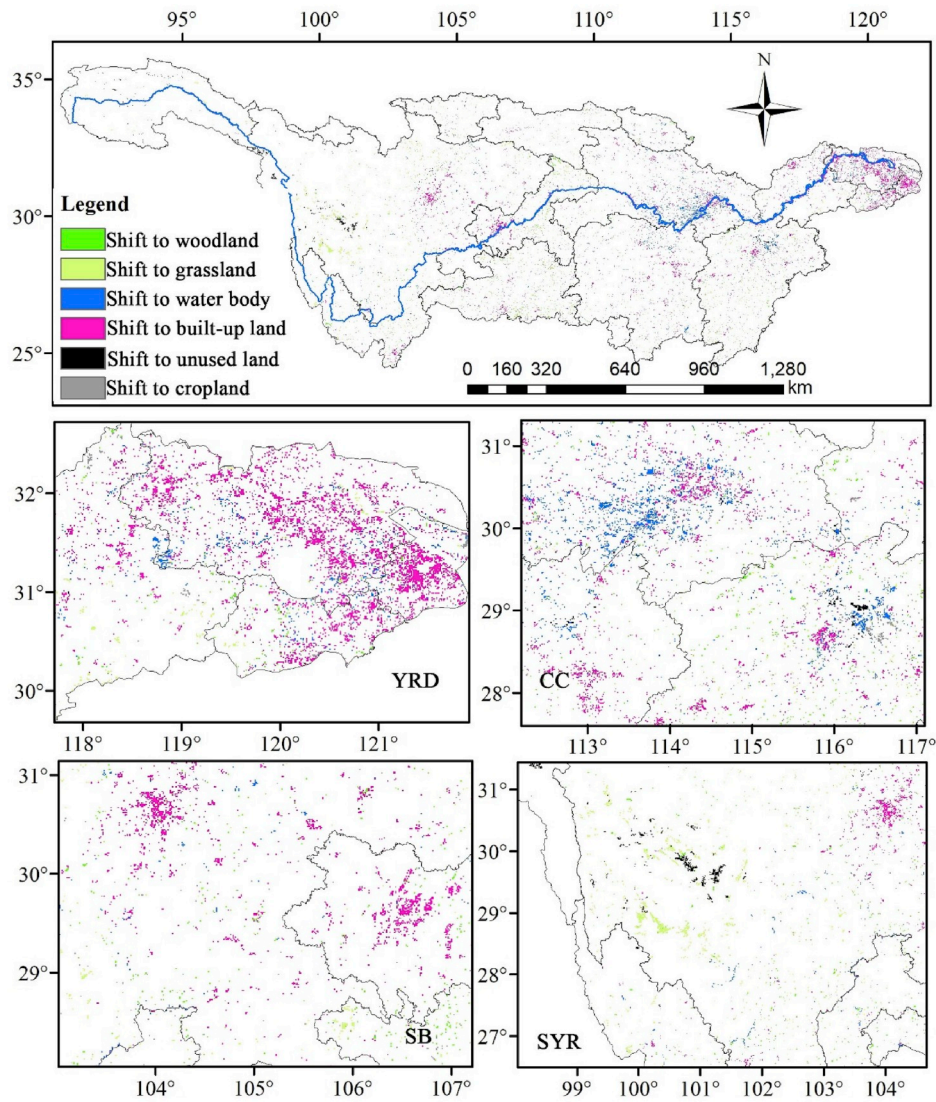
Fig. 8. Six primary land use shift trajectories in the YRB from 1980 to 2015.

Table 4
LUCCs of the YRB from 1980 to 2010 (%).

	Cropland	Woodland	Grassland	Water body	Built-up land	Unused land
Cropland	93.147	0.519	0.237	0.957	**5.119**	0.021
Woodland	0.249	99.088	0.449	0.057	0.140	0.017
Grassland	0.280	0.803	98.731	0.079	0.045	0.061
Water Body	1.903	0.384	3.978	89.882	0.444	3.408
Built-up land	0.012	0.012	0.024	0.146	99.793	0.012
Unused land	0.172	0.058	0.368	1.245	0.038	98.119
Change rate (%)	2.616	1.776	5.056	2.484	**5.786**	3.519

Table 5
LUCC of the YRB from 2010 to 2015 (%).

	Cropland	Woodland	Grassland	Water body	Built-up land	Unused land
Cropland	98.566	0.088	0.033	0.137	**1.170**	0.007
Woodland	0.038	99.622	0.081	0.028	0.229	0.002
Grassland	0.026	0.058	99.766	0.045	0.101	0.004
Water Body	0.346	0.067	0.158	98.908	0.453	0.067
Built-up land	0.595	0.190	0.042	0.131	99.034	0.008
Unused land	0.002	0.002	0.002	0.236	0.005	99.752
Change rate (%)	1.007	0.405	0.316	0.577	**1.958**	0.088

Table 6
Regression coefficients of AOD, ADRE and urban form metrics using MLR model.

	AOD	$|ADRE_{TOA}|$	$|ADRE_{SFC}|$	$ADRE_{ATM}$
CA	2.019E-7**	2.882E-6**	4.340E-6***	1.462E-6**
NP	6.778E-5***	0.001***	0.002**	0.002***
LPI	−0.09**	−0.125**	−0.385**	−0.26**
ED	0.23**	0.363**	0.99**	0.627**
PGDP	−1.522E-7*	−2.636E-6	−4.495E-6*	−1.858E-6*
PD	6.295E-5***	0.001***	0.003***	0.002**
Prec	−0.08**	−0.054	−0.558*	−0.612
T	0.35***	0.583*	1.245***	0.662**
Constant	−9.584	−158.646***	−336.699***	−178.048***
Adjusted-R^2	0.726	0.692	0.688	0.682
Observations	121	121	121	121

*P < 0.1, **P < 0.05, ***P < 0.01.

form metrics based on GWR model. Obviously, the high determination coefficients ($R^2 > 0.5$) were concentrated in the SYR, indicating that the changes of urban from metrics could explain more than 50% of the AOD changes in this region. However, the low R^2 (<0.1) mainly appeared in the middle and lower reaches of the YRB. It suggested that the fitting degree of GWR model was poor in this area, and changes in urban from metrics could only explain less than 10% of AOD changes. The reason might be that there were various aerosol sources in the middle and lower reaches of the YRB, which weakened the impact of urban form on the aerosols.

Fig. 10 showed the regression coefficients of AOD and urban form metrics in 121 cities of the YRB from 1980 to 2015 by using the GWR model. In most areas of the YRB, AOD was positively correlated with CA, NP and ED, but negatively related to LPI. The results were consistent with the correlations estimated by the MLR model. However, there was a spatial differentiation of the correlations between AOD and urban forms. For example, some negative correlations between AOD and CA occurred in the SYR. The increase of CA in the SYR was mainly due to the development of tourism rather than the expansion in industrial and mineral land (Wei et al., 2015). As a result, a large number of aerosol emissions did not occur. In addition, the positive correlation between AOD and NP weakened gradually from east to west. Conversely, the positive correlation between AOD and ED showed a trend of increasing from east to west. The negative correlation between AOD and LPI increased gradually from west to east. Fig. S5 further showed the regression coefficients between ADRE and urban form metrics using the GWR model. As observed, the correlations between ADRE and urban forms were spatially consistent with those of AOD and urban forms.

3.5. Effect of meteorological conditions on AOD and ADRE trends

Fig. 11 showed the determination coefficients between AOD and meteorological metrics obtained using the MLR model. As observed,

high R^2 (>0.5) values were observed over the SYR in spring and summer, suggesting that changes in meteorological conditions could explain up to 50% of AOD changes in the SYR. Several reasons could account for this phenomenon. One was probably due to the unique plateau climate in the SYR. Another was due to the low population density and infrequent industrial activities in the SYR. As a result, the impact of anthropogenic factors on aerosols was relatively low, which in turn strengthened the impact of local meteorological conditions on aerosols.

Fig. 12 showed the regression coefficients between AOD and six meteorological factors. Red (green) grids were positive (negative) correlations. As observed in Fig. 12 (β_1), over most areas of the YRB, AOD was negatively related to surface wind speed. High wind speed facilitated circulation and dilution of aerosols (Tai et al., 2010). However, there was a positive correlation between AOD and surface wind speed over the SYR. To clarify the reasons, we further calculated the 72-h backward trajectory of 500m, 1000m and 3000m altitudes using the NOAA HYSPLIT model (Fig. 13). The end point was at 20:00 (GMT) on April 25, 2014 and from the source of YRB (33.02°N, 94.87°E). As observed, dust aerosols from Taklimakan Desert were transmitted into the SYR at all three altitudes of 500m, 1000m and 3000m under the action of wind. As a result, a positive AOD-wind correlation occurred in the SYR. Similarly, Munir et al. (2017) also found that fine-mode aerosols were positively related to wind speed in Arid Saudi Arabia. Fig. 12 (β_2) showed a positive correlation between AOD and surface temperature in the whole YRB. The reason probably was that the oxidation of aerosol precursors (such as sulfur dioxide) could be enhanced at high temperature (Westervelt et al., 2016). Fig. 12 (β_3) found that AOD was negatively related to precipitation except for the SYR, mainly due to the scouring effect of precipitation. In Fig. 12 (β_4) - (β_5), the relationship of relative humidity (RH) and total cloud cover with $PM_{2.5}$ showed a regional dependency, with the positive correlation in the SYR. The reason was associated with the hygroscopic growth of aerosols (Yang et al., 2017). However, in the southern part of the YRB, AOD had a weak negative correlation with RH. Yang et al. (2017) analyzed that if RH > 80%, rainfall events would occur frequently, thereby scouring aerosols in the atmosphere. As shown in Fig. S6, the relative humidity was as high as 85% in summer over the southern part of the YRB, thereby scouring aerosols with frequent occurrence of rainfall events. Fig. 12 (β_6) showed a significant negative correlation between AOD and Boundary Layer Height (BLH). This was because a well-developed boundary layer was conducive to aerosol diffusion (Wang et al., 2018).

Fig. 14 showed the annual mean trends of six meteorological factors from 1980 to 2016. Black dots represented those trends above 95% significance level (p < 0.05). Obviously, in most areas of the YRB, there were no significant trends in surface wind speed, precipitation, RH, total cloud cover and BLH. It suggested that although the local meteorological conditions were associated with seasonal variations of AOD, changes in these meteorological metrics were unlikely to be the main factor for the
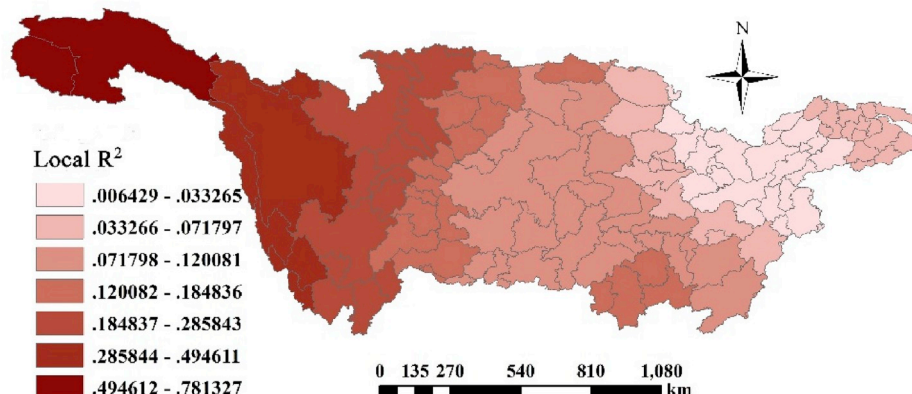

Fig. 9. Local coefficients of determination (R^2) of AOD and urban form metrics based on GWR model.
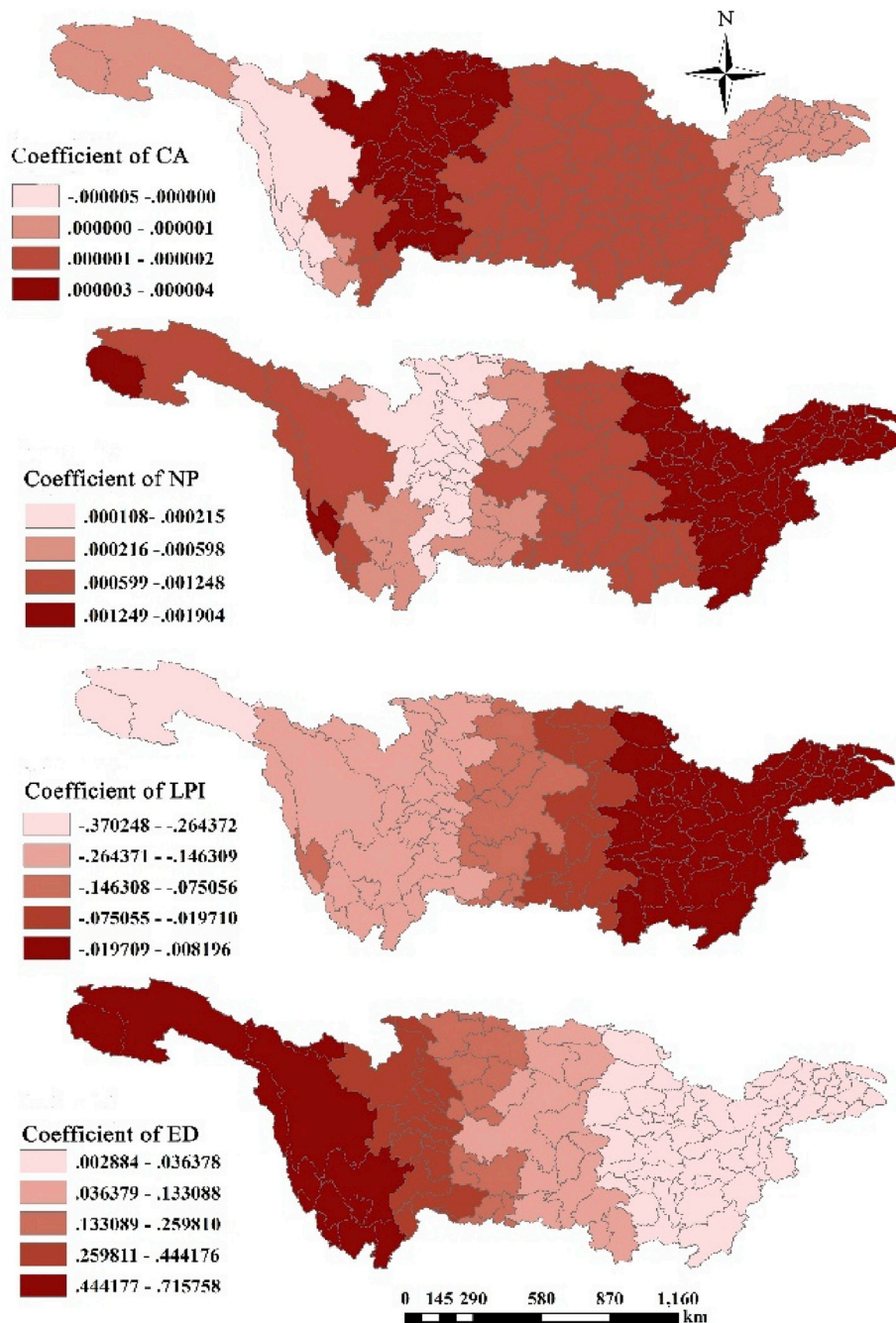
Fig. 10. Regression coefficients of AOD and urban form metrics based on GWR model.

growth of AOD in the YRB from 1980 to 2016. However, there was a significant upward trend in temperature, with an average annual growth rate of 0.003 K yr^{-1}. Furthermore, as observed in Fig. 12, temperature was positively related to AOD and its regional average regression coefficient (β_2) was about 0.28 K^{-1}. Therefore, a growth of 0.003 K yr^{-1} in temperature would theoretically increase AOD by 0.00084 yr^{-1}. But in fact, the average annual growth of AOD in the YRB from 1980 to 2016 was about 0.0065 yr^{-1}, which was much larger than the theoretical value (0.00084 yr^{-1}). It suggested that the effect of the temperature rise on AOD trend was lower than the impact of anthropogenic emissions on AOD trend (Westervelt et al., 2016).

4. Conclusions and policy implications

Since the reform and opening up, the Yangtze River Basin (YRB)

underwent rapid urbanization and industrialization, and it has now become the most important source of anthropogenic aerosol emissions in the word. This study was conducted to analyze the quantitative impact of anthropogenic and meteorological factors on AOD and ADRE trends since 1980, with respect to anthropogenic emissions, land use cover changes, urban forms and meteorological conditions. The main conclusions are presented in the following:

Results revealed that over the entire YRB, aerosols had a cooling effect at the top of atmosphere and at the surface but a warming effect within the atmosphere. Furthermore, there were significant upwards trends in AOD, |ADRE$_{TOA}$|, |ADRE$_{SFC}$|, and ADRE$_{ATM}$ over the YRD, CC, and SB during 1980–2016, but not over the SYR. Notably, these over-increasing AOD and ADRE trends were curbed around 2010. During 2010–2016, the annual mean downward trends of AOD, |ADRE$_{TOA}$|, |ADRE$_{SFC}$|, and ADRE$_{ATM}$ were −0.02 year^{-1}, -0.33 Wm^{-2} year^{-1}, -0.65
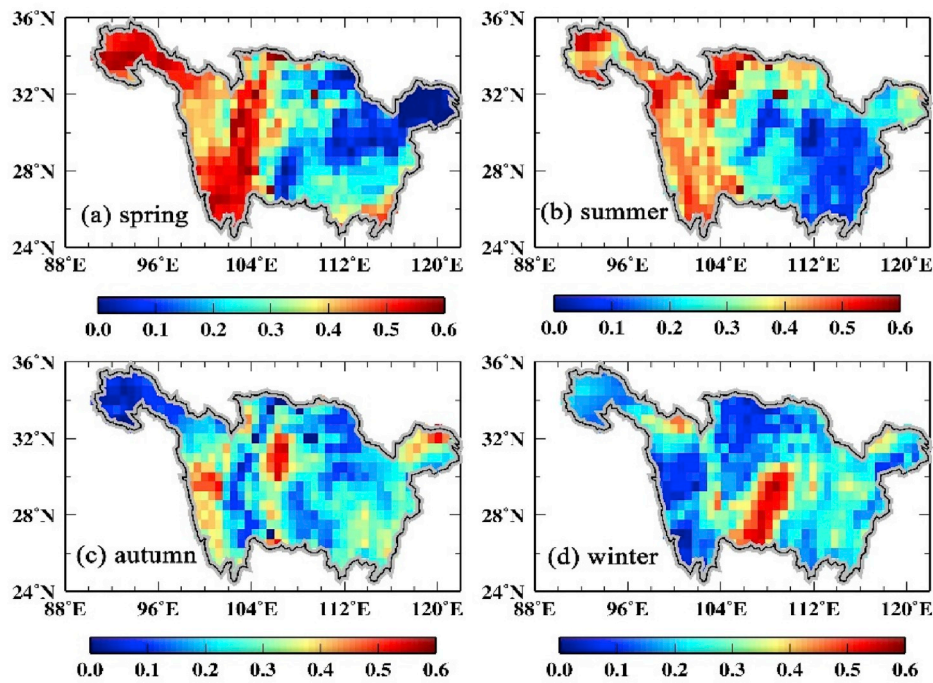
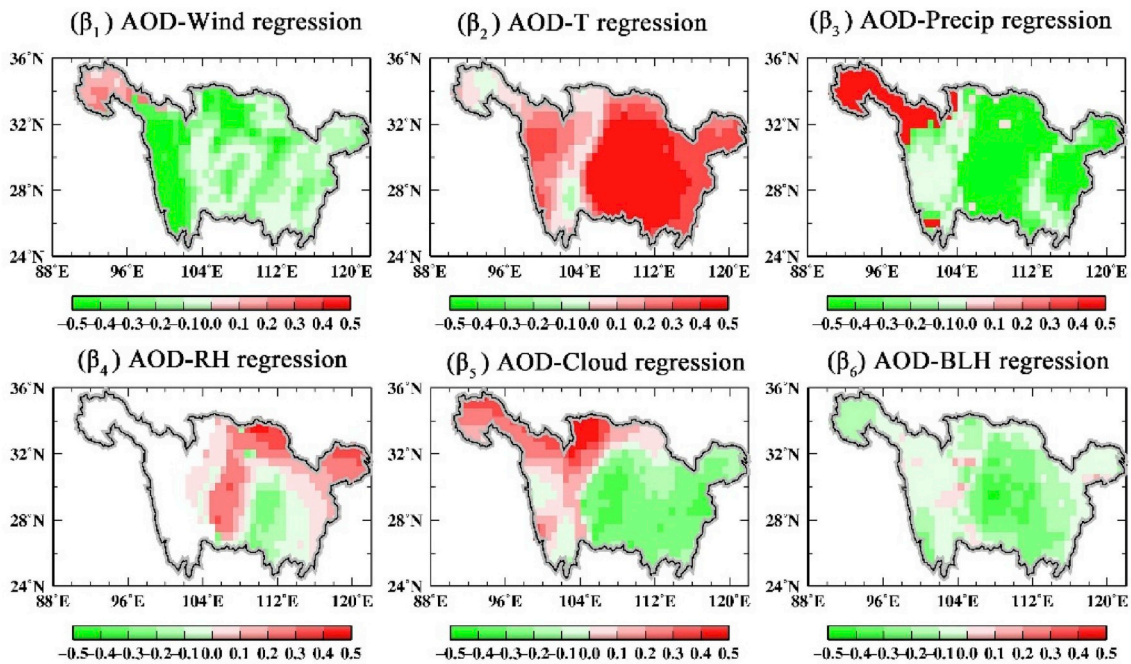**Fig. 11.** Determination coefficients (R^2) of AOD and six meteorological metrics.

Fig. 12. Regression coefficients for AOD and meteorological conditions determined using MLR model.

Wm^{-2} year^{-1}, and -0.36 Wm^{-2} year^{-1}, respectively. However, it is not yet known whether this downward trend is temporary or sustained and therefore requires long-term future observations of terrestrial and satellite data.

With respect to anthropogenic emissions (BC, OC, SO$_2$, and SO$_4$), AOD and ADRE were significantly positively related to these anthropogenic emissions in the middle and lower reaches of the YRB. However, there was no significant correlation in the SYR. From the perspective of LUCC, AOD and ADRE were closely related to land use types. Specifically, the AOD and ADRE values were largest for built-up land and cropland, followed by water bodies and woodland, but values were the lowest for grassland and unused land. In addition, LUCC had a significant impact on the changes of AOD and ADRE. During 1980–2010, the YRD, CC and SB experienced a rapid expansion of built-up land, with an increasing rate of 5.79%. As a result, it led to a significant growth of AOD and ADRE in this region. However, during 2010–2015, the conversion from cropland to built-up land was much less (1.17%), thus effectively preventing the excessive growth of AOD and ADRE during this period. From the perspective of urban forms, AOD and ADRE were found to be positively correlated with patch area (CA), patch number (NP), and patch edge density (ED), but negatively related to the largest patch index (LPI). It suggested that a compact urban form could alleviate aerosol

NOAA HYSPLIT MODEL
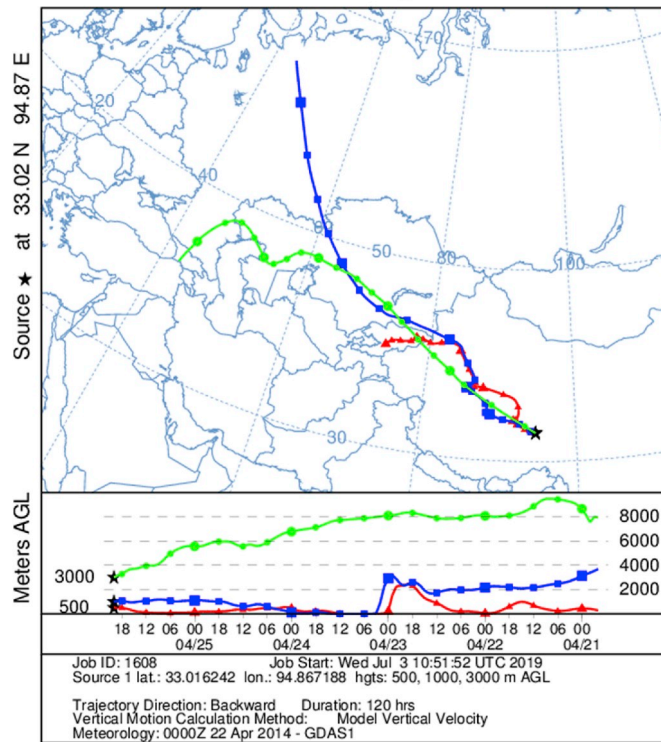Backward trajectories ending at 2000 UTC 25 Apr 14
GDAS Meteorological Data

Fig. 13. A 72-h backward trajectory of 500m (red), 1000m (blue) and 3000m (green) altitudes at 20:00 (GMT) on April 25, 2014. (For interpretation of the references to colour in this figure legend, the reader is referred to the Web version of this article.)
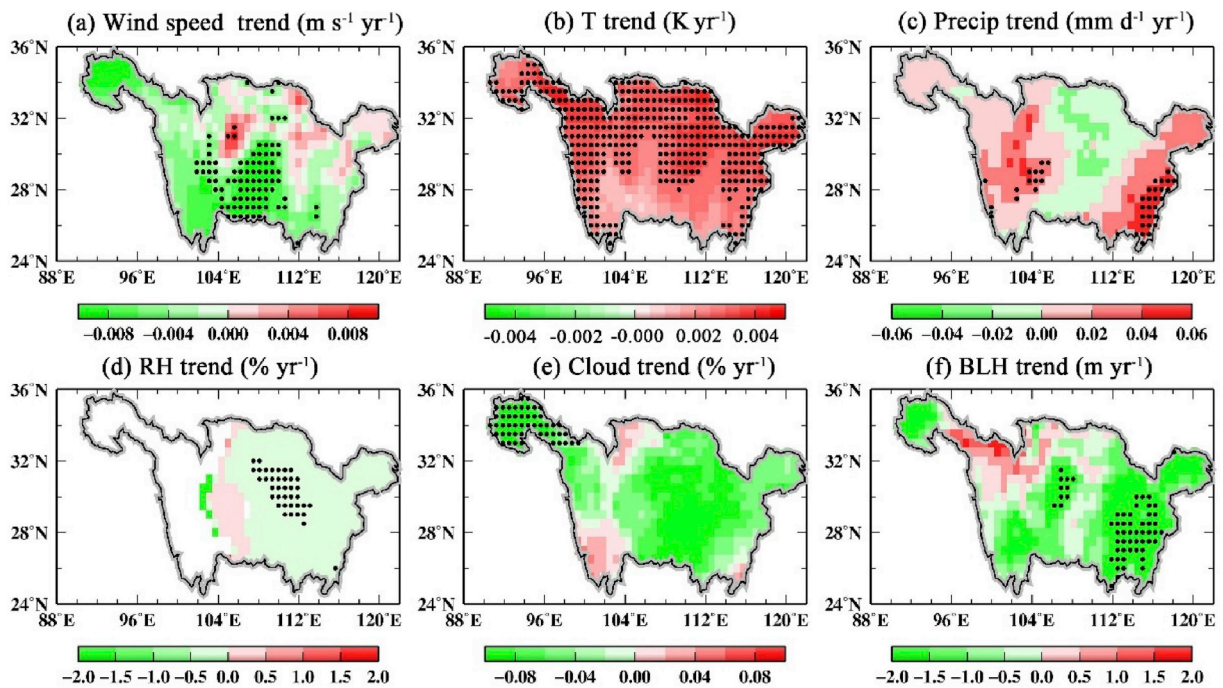

Fig. 14. Annual mean trends in six meteorological factors from 1980 to 2016.

pollution by enhancing urban connectivity and reducing vehicle dependence.

Seasonal variations in AOD were seen to be closely associated with local meteorological conditions. However, these meteorological metrics had no significant trends, except temperature. It indicated that meteorological changes were unlikely to be the main reason for 1980–2016 trend of AOD. Notably, there was a significantly increasing trend in temperature, with an annual growth rate of 0.003 K year^{-1}. It indicated that the temperature rise was one of the driving factors for the significant growth of AOD, but its impact was far less than the impact of anthropogenic emissions.

This study could help decision makers alleviate aerosol pollution from the perspectives of reducing anthropogenic emissions, developing compact urban forms and controlling temperature rise. Furthermore, remarkable regional differences were observed with respect to the effects of anthropogenic and meteorological factors on aerosol trends. For example, anthropogenic emissions were found to be closely related to AOD-ADRE in the middle and lower reaches of the YRB, but failed in the SYR. Conversely, six meteorological metrics could explain up to 50% of AOD changes in the SYR. In this regard, decision makers need to adequately consider regional differences in anthropogenic and meteorological conditions to ensure mitigation of aerosol loading and avoid a "one size fits all" approach.

CRediT author statement

Lijie He: Data curation, Writing- Original draft preparation, revision.
Lunche Wang: Conceptualization, Methodology, Software , Reviewing and Editing, Supervision, Project administration, Funding acquisition.
Bo Huang: Methodology, Supervision, Project administration.
Wei Jing: Visualization, Investigation.
Zhigao Zhou: Software, Validation.
Yang Zhong: Editing.

Declaration of competing interest

The authors declare that they have no known competing financial interests or personal relationships that could have appeared to influence the work reported in this paper.

Acknowledgements

Appendix A. Supplementary data

Supplementary data to this article can be found online at https://doi.org/10.1016/j.atmosenv.2019.117188.

References

Alfaro–Contreras, R., Zhang, J., Reid, J.S., Sundar, C., 2017. A study of 15–year aerosol optical thickness and direct shortwave aerosol radiative effect trends using MODIS, MISR, CALIOP and CERES. Atmos. Chem. Phys. 17, 13849. https://doi.org/10.5194/acp-17-13849-2017.

Buchard, V., Randles, C.A., da Silva, A.M., Darmenov, A., Colarco, P.R., Govindaraju, R., Ferrare, R., Hair, J., Beyersdorf, A.J., Ziemba, L.D., Yu, H., 2017. The MERRA–2 aerosol reanalysis, 1980 onward. Part II: evaluation and case studies. J. Clim. 30, 6851–6872.

Clark, L.P., Millet, D.B., Marshall, J.D., 2011. Air quality and urban form in US urban areas: evidence from regulatory monitors. Environ. Sci. Technol. 45, 7028–7035.

Che, H., Xia, X., Zhao, H., Dubovik, O., Holben, B.N., Goloub, P., Qi, B., 2019. Spatial distribution of aerosol microphysical and optical properties and direct radiative effect from the China Aerosol Remote Sensing Network. Atmos. Chem. Phys. 19, 11843–11864.

De Leeuw, G., Sogacheva, L., Rodriguez, E., Kourtidis, K., Georgoulias, A.K., Alexandri, G., Amiridis, V., Proestakis, E., Marinou, E., Xue, Y., 2017. Two decades of satellite observations of AOD over mainland China. Atmos. Chem. Phys. Discuss. 2017, 1–33.

Deng, X., Tie, X., Zhou, X., Wu, D., Zhong, L., Tan, H., Deng, T., 2008. Effects of Southeast Asia biomass burning on aerosols and ozone concentrations over the Pearl River Delta (PRD) region. Atmos. Environ. 42 (36), 8493–8501.

Dutton, E.G., Christy, J.R., 1992. Solar radiative forcing at selected locations and evidence for global lower tropospheric cooling following the eruptions of El Chichón and Pinatubo. Geophys. Res. Lett. 19, 2313–2316.

Fan, C., Tian, L., Zhou, L., Hou, D., Song, Y., Qiao, X., Li, J., 2018. Examining the impacts of urban form on air pollutant emissions: evidence from China. J. Environ. Manag. 212, 405–414.

Gao, Y., Liu, X., Zhao, C., Zhang, M., 2011. Emission controls versus meteorological conditions in determining aerosol concentrations in Beijing during the 2008 Olympic Games. Atmos. Chem. Phys. 11 (23), 12437–12451.

Ge, Y., Zhang, K., Yang, X., 2019. A 110-year pollen record of land use and land cover changes in an anthropogenic watershed landscape, eastern China: understanding past human-environment interactions. Sci. Total Environ. 650, 2906–2918.

Guo, J., He, J., Liu, H., Miao, Y., Liu, H., Zhai, P., 2016. Impact of various emission control schemes on air quality using WRF-Chem during APEC China 2014. Atmos. Environ. 140, 311–319.

He, L., Lin, A., Chen, X., Zhou, H., Zhou, Z., He, P., 2019a. Assessment of MERRA-2 surface PM2. 5 over the Yangtze River basin: ground-based verification, spatiotemporal distribution and meteorological dependence. Remote Sens. 11 (4), 460. https://doi.org/10.3390/rs11040460.

He, L., Liu, Y., He, P., Zhou, H., 2019b. Relationship between air pollution and urban forms: evidence from prefecture-level cities of the Yangtze River basin. Int. J. Environ. Res. Public Health 16 (18), 3459. https://doi.org/10.3390/ijerph16183459.

He, L., Wang, L., Lin, A., Zhang, M., Bilal, M., Tao, M., 2017. Aerosol optical properties and associated direct radiative forcing over the Yangtze River basin during 2001–2015. Remote Sens. 9, 746. https://doi.org/10.3390/rs9070746.

He, L., Wang, L., Lin, A., Zhang, M., Bilal, M., Wei, J., 2018a. Performance of the NPP–VIIRS and aqua–MODIS aerosol optical depth products over the Yangtze River basin. Remote Sens. 10, 117. https://doi.org/10.3390/rs10010117.

He, L., Wang, L., Lin, A., Zhang, M., Xia, X., Tao, M., Zhou, H., 2018b. What drives changes in aerosol properties over the Yangtze River Basin in past four decades? Atmos. Environ. 190, 269–283.

He, Q., Zhang, M., Huang, B., 2016. Spatio–temporal variation and impact factors analysis of satellite–based aerosol optical depth over China from 2002 to 2015. Atmos. Environ. 129, 79–90.

IPCC, 2013. Climate change 2013: the physical science basis. In: Stocker, T.F., Qin, D., Plattner, G.-K., Tignor, M., Allen, S.K., Boschung, J., Nauels, A., Xia, Y., Bex, V., Midgley, P.M. (Eds.), Contribution of Working Group I to the Fifth Assessment Report of the Intergovernmental Panel on Climate Change. Cambridge University Press, Cambridge, United Kingdom and New York, NY, USA, p. 1535.

Kuang, Y., Zhao, C.S., Tao, J.C., Ma, N., 2015. Diurnal variations of aerosol optical properties in the North China Plain and their influences on the estimates of direct aerosol radiative effect. Atmos. Chem. Phys. 15, 5761–5772.

Kuang, Y., Zhao, C.S., Tao, J.C., Bian, Y.X., Ma, N.J.A.E., 2016. Impact of aerosol hygroscopic growth on the direct aerosol radiative effect in summer on North China Plain. Atmos. Environ. 147, 224–233.

Larkin, A., van Donkelaar, A., Geddes, J.A., Martin, R.V., Hystad, P., 2016. Relationships between changes in urban characteristics and air quality in East Asia from 2000 to 2010. Environ. Sci. Technol. 50, 9142–9149.

Li, L., Wang, Y., 2014. What drives the aerosol distribution in Guangdong–the most developed province in Southern China? Sci. Rep. 4, 5972. https://doi.org/10.1038/srep05972.

Liu, J., Liu, M., Tian, H., Zhuang, D., Zhang, Z., Zhang, W., Deng, X., 2005. Spatial and temporal patterns of China's cropland during 1990–2000: an analysis based on Landsat TM data. Remote Sens. Environ. 98 (4), 442–456.

Liu, Q., Wang, S., Zhang, W., Li, J., Dong, G., 2019. The effect of natural and anthropogenic factors on PM2. 5: empirical evidence from Chinese cities with different income levels. Sci. Total Environ. 653, 157–167.

McCarty, J., Kaza, N., 2015. Urban form and air quality in the United States. Landsc. Urban Plan. 139, 168–179.

Munir, S., Habeebullah, T.M., Mohammed, A.M., Morsy, E.A., Rehan, M., Ali, K., 2017. Analyzing PM2.5 and its association with PM10 and meteorology in the arid climate of Makkah, Saudi Arabia. Aerosol Air Qual. Res. 17, 453–464.

Randles, C.A., da Silva, A.M., Buchard, V., Colarco, P.R., Darmenov, A., Govindaraju, R., Smirnov, A., Holben, B., Ferrare, R., Hair, J., Shinozuka, Y., 2017. The MERRA–2 aerosol reanalysis, 1980 onward. Part I: system description and data assimilation evaluation. J. Clim. 30, 6823–6850.

Remer, L.A., Kaufman, Y.J., 2006. Aerosol direct radiative effect at the top of the atmosphere over cloud free ocean derived from four years of MODIS data. Atmos. Chem. Phys. 6 (1), 237–253.

Rodríguez, M.C., Dupont-Courtade, L., Oueslati, W., 2016. Air pollution and urban structure linkages: evidence from European cities. Renew. Sustain. Energy Rev. 53, 1–9.

She, Q., Peng, X., Xu, Q., Long, L., Wei, N., Liu, M., Xiang, W., 2017. Air quality and its response to satellite-derived urban form in the Yangtze River Delta, China. Ecol. Indicat. 75, 297–306.

Tai, A.P., Mickley, L.J., Jacob, D.J., 2010. Correlations between fine particulate matter (PM2.5) and meteorological variables in the United States: implications for the sensitivity of PM2. 5 to climate change. Atmos. Environ. 44 (32), 3976–3984.

Wang, L., Gong, W., Xia, X., Zhu, J., Li, J., Zhu, Z., 2015. Long–term observations of aerosol optical properties at Wuhan, an urban site in Central China. Atmos. Environ. 101, 94–102.

Wang, S., Liu, X., Zhou, C., Hu, J., Ou, J., 2017. Examining the impacts of socioeconomic factors, urban form, and transportation networks on CO2 emissions in China's megacities. Appl. Energy 185, 189–200.

Wang, X., Dickinson, R.E., Su, L., Zhou, C., Wang, K., 2018. PM2. 5 pollution in China and how it has been exacerbated by terrain and meteorological conditions. Bull. Am. Meteorol. Soc. 99, 105–119.

Wang, X., Zhang, F., Jing, Y., Zhang, H., Li, Z., 2016. Relationship between land cover-landscape spatial characteristics and aerosol optical depth in Ebinur Lake Watershed. Trans. Chin. Soc. Agric. Eng. 32 (22), 273–283. https://doi.org/10.11975/j.issn.1002-6819.2016.22.038 (in Chinese).

Wei, J., Huang, W., Li, Z., Xue, W., Peng, Y., Sun, L., Cribb, M., 2019a. Estimating 1-km-resolution PM$_{2.5}$ concentrations across China using the space-time random forest approach. Remote Sens. Environ. 231, 111221. https://doi.org/10.1016/j.rse.2019.111221.

Wei, J., Li, Z., Guo, J., Sun, L., Huang, W., Xue, W., Fan, T., Cribb, M., 2019b. Satellite-derived 1-km-resolution PM$_1$ concentrations from 2014 to 2018 across China. Environ. Sci. Technol. 53, 13265–13274.

Wei, J., Peng, Y., Mahmood, R., Sun, L., Guo, J., 2019c. Intercomparison in spatial distributions and temporal trends derived from multi-source satellite aerosol products. Atmos. Chem. Phys. 19, 7183–7207. https://doi.org/10.5194/acp-19-7183-2019.

Westervelt, D.M., Horowitz, L.W., Naik, V., Tai, A.P.K., Fiore, A.M., Mauzerall, D.L., 2016. Quantifying PM$_{2.5}$-meteorology sensitivities in a global climate model. Atmos. Environ. 142, 43–56.

Xia, X., Che, H., Zhu, J., Chen, H., Cong, Z., Deng, X., Fan, X., Fu, Y., Goloub, P., Jiang, H., Liu, Q., 2016. Ground–based remote sensing of aerosol climatology in China: aerosol optical properties, direct radiative effect and its parameterization. Atmos. Environ. 124, 243–251.

Yang, Y., Russell, L.M., Lou, S., Liao, H., Guo, J., Liu, Y., Ghan, S.J., 2017. Dust-wind interactions can intensify aerosol pollution over eastern China. Nat. Commun. 8, 15333. https://doi.org/10.1038/ncomms15333.

Zhang, J., Reid, J.S., Alfaro-Contreras, R., Xian, P., 2017. Has China been exporting less particulate air pollution over the past decade? Geophys. Res. Lett. 44 (6), 2941–2948.

Zhou, H., Luo, Z., Tangdamrongsub, N., Wang, L., He, L., Xu, C., Li, Q., 2017. Characterizing drought and flood events over the Yangtze River basin using the HUST–grace2016 solution and ancillary data. Remote Sens. 9, 1100. https://doi.org/10.3390/rs9121200.

Zhou, H., Luo, Z., Zhou, Z., Li, Q., Zhong, B., Lu, B., Hsu, H., 2018. Impact of different kinematic empirical parameters processing strategies on temporal gravity field model determination. J. Geophys. Res. Sol. Ea. 123 (11), 10–252.